



# Experimental lifetime study of regeneratively cooled rocket chamber walls

Felix Hötte<sup>a,\*</sup>, Christoph v. Sethe<sup>b</sup>, Torben Fiedler<sup>c</sup>, Matthias C. Haupt<sup>a</sup>, Oskar J. Haidn<sup>b</sup>, Michael Rohdenburg<sup>a</sup>

<sup>a</sup> TU Braunschweig, Institute for Aircraft Design and Lightweight Structures, Hermann-Blenk-Str. 35, Germany

<sup>b</sup> TU München, Chair of Turbomachinery and Flight Propulsion, Boltzmannstrasse 15, Germany

<sup>c</sup> TU Braunschweig, Institute for Materials, Langer Kamp 8, Germany

## ARTICLE INFO

### Keywords:

Thermomechanical fatigue/cycling  
Aerospace  
Plasticity  
Corrosion fatigue  
Copper alloys

## ABSTRACT

A detailed knowledge of the life-limiting mechanisms of regeneratively cooled rocket combustion chambers is important to increase the safety, the thrust-to-weight ratio and the cost-efficiency of future rocket engines. For this purpose, an actively cooled specimen made of CuCr1Zr is mounted downstream of a combustion chamber. The specimen is loaded cyclically and inspected after each cycle. The specimens collapse in the 'doghouse' failure mode after several load cycles. The effects of different hot-gas and coolant conditions, surface roughness and thermal barrier coatings on the lifetime are studied. The life-limiting mechanisms: creeping, yielding, abrasion, blanching and thermal aging are discussed.

## 1. Introduction

Regeneratively cooled structures of rocket engines are extremely loaded. The loads are caused by the interactions of the hot combustion gas (around 3500 K for CH<sub>4</sub>/OX) and cold cooling channel flows (around 100 K for LCH<sub>4</sub>), which leads to large temperature gradients and a high level of temperature in the structure (up to around 1000 K for copper alloys) in combination with high pressure differences between both fluids. This study aims for a better understanding of the physical behavior of the three main components: structure, hot-gas and coolant flows, and their interactions, especially the lifetime of the structure.

Some lifetime experiments on combustion chamber structures have been conducted since the 1970s. Quentmeyer has investigated the low-cycle thermal fatigue of 21 cylindrical, LH<sub>2</sub> cooled test sections of a GH<sub>2</sub>/LOX combustor [1]. Inside of the sub-scale combustion chamber a water-cooled centerbody was installed to reduce the consumption of fuel and to form the combustion, sonic throat and expansion region of a rocket engine. Three different materials were studied. Thermocouples were placed in the cooling channel ribs and in the inlet and outlet manifold of the coolant. The tests were performed at a chamber pressure of 41.4 bar and a mixture ratio (oxygen to fuel ratio) of 6.0. The heat flux in the throat region reached 54 MW/m<sup>2</sup>. The tests were repeated cyclically until a combustion chamber failure was detected by sensing a coolant passage leak. The deformations of the hot-gas wall were not investigated quantitatively. Neither individual coolant mass

flow rate measurements nor mass flow rate control were performed.

Jankovsky et al. have used the same test setup [2]. They have investigated the lifetime of two combustion chambers with tubular cooling channels and have compared them with those with rectangular cooling channels.

The same test setup was also used for the study of Pavli et al. [3]. Therein, the lifetime of two compliant combustion chambers were investigated. Gaps between the cooling channel walls allowed a free thermal expansion of the material in circumferential direction. It was found that the lifetime was significantly increased due to the strong reduction of the alternating tensing and compressing yields (thermal ratcheting).

Anderson et al. have placed a catalyst bed upstream of a sub-scale combustion chamber [4]. The catalyst bed decomposed H<sub>2</sub>O<sub>2</sub> into H<sub>2</sub>O and O<sub>2</sub>. Adding JP-8 (aviation turbine fuel) to these gases in a gas generator has produced a well-mixed hot-gas of known temperature and composition which was then fed into the test section. The section consisted of a water-cooled copper liner with a stainless steel jacket and a diverging centerbody, which formed the throat. The test section was equipped with differential pressure sensors, calorimeters and thermocouples. The chamber pressure during the cyclic load phases was 13.8 bar. Between the cycles the entire test section was disassembled to investigate the deformations. An unexpected failure occurred after around 100 cycles, presumably caused by an unequal distribution of the coolant to the channels.

Kimura et al. have used a new LOX/LH<sub>2</sub> reusable rocket engine in

\* Corresponding author.

E-mail address: [f.hoette@tu-braunschweig.de](mailto:f.hoette@tu-braunschweig.de) (F. Hötte).

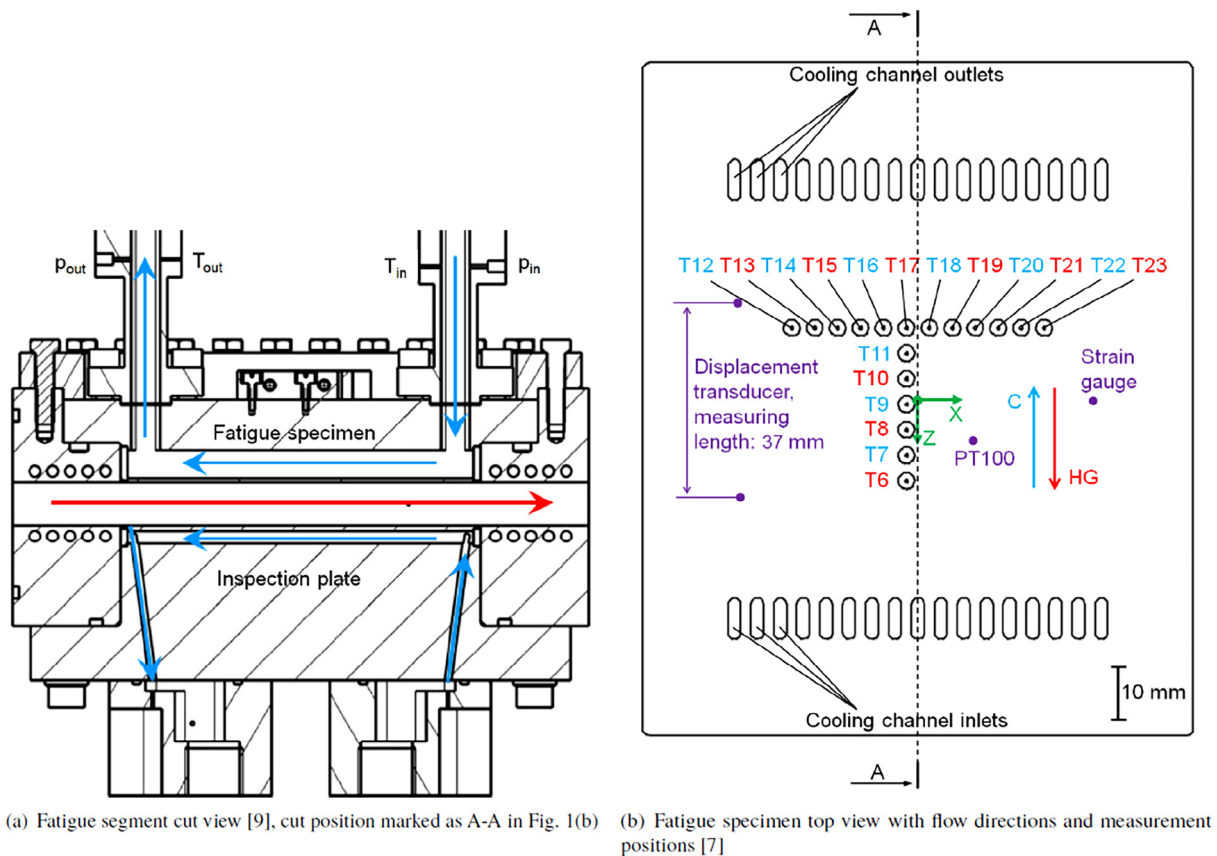


Fig. 1. Experimental setup.

full-scale to prove the lifetime [5]. During the load cycles the chamber pressure reached a maximum of 16–34 bar in a mixture ratio range of 6.0–6.2. After in total 54 hot tests with in total 142 load cycles no apparent damage was detected.

In Thiede et al. flat specimen with five cooling channels, which represent small sections of combustion chamber walls, were heated by laser irradiation instead of hot-gas flow [6]. The laser allowed heat fluxes up to 20 MW/m<sup>2</sup>. The specimen were sandwich structures with a CuCr1Zr core and galvanic nickel face sheets. During the tests the temperature and deformation of the laser-heated side were measured by an infrared camera and a stereo camera system. Additionally, in every cooling channel before and after the specimen, the temperature and the pressure of the coolant (nitrogen) flow were measured. The coolant temperature of 160 K was obtained by mixing liquid and gaseous nitrogen. The mass flow was measured and controlled individually for every channel. After 174 load cycles the TMF panel cracked in the middle cooling channel.

A study of the thermo-mechanical fluid–structure interaction of rocket combustion chambers was presented in [7]. In the present paper, the same experimental setup is used to study the lifetime of rocket chamber walls. Therein, a fatigue segment is placed downstream of a five injector element GOX-GCH<sub>4</sub> rectangular sub-scale combustor at an  $L^* = 0.717$  m, which is sufficient to justify the assumption of complete combustion. A special aim is to reproduce the so called doghouse effect, a structural failure mode of rocket combustion chambers which is caused by cyclic, thermo-mechanical loading. The test section includes a fatigue specimen with 17 high aspect ratio cooling channels. The specimen is loaded cyclically. The novel approach is the use of a combustion chamber with rectangular cross section and a replaceable specimen with individually controlled cooling flow through each of the cooling channels combined with the hot-gas flow. This leads to the possibility of detailed deformation and roughness inspections under

well defined and realistic conditions. In contrast to the hot-gas experiments described in the aforementioned literature, the deformations of the hot-gas wall are determined quantitatively and after each cycle. Because of that the results can be also used for validation of numerical simulations as described for example in [8]. The design process of the fatigue experiment is explained in [9].

In comparison to the previous test campaigns A and B, which are described in detail in [7], in the actual campaigns C-K much less combustion instabilities occurred. In campaigns C-G the chamber pressure was increased by 10% to accelerate the thermo-mechanical fatigue by higher temperatures and heat fluxes, whereas the cooling conditions were not changed. In campaigns C and D the default design of the fatigue specimen was tested, whereas in Campaign E a fatigue specimen with a higher initial surface roughness was used.

In campaigns F and G fatigue specimen with thermal barrier coatings were used. The thermal barrier coatings were tested in previous work in high-power laser cycling experiments [10]. These experiments led to a broad understanding of different failure modes of coatings in rocket combustion chambers, but tests with a realistic hot-gas flow could not be performed so far. For the present study, a thermal barrier coating system designed for full-scale engines was used to test the effect of hot-gas flow on the coating failure, especially on the growth of vertical cracks that are supposed to be inevitable in rocket combustion chambers. In the previous work [10] was found that these cracks can be tolerated as long as they do not propagate into the substrate or along the substrate/coating interface.

In campaigns H - K the chamber pressure and the coolant mass flow were increased by 50%. The coolant pressure was increased from 70 bar to 80 bar to achieve the same pressure difference between hot-gas and coolant during the main stage of the fire phase as in the previous tests. In addition, the duration of the combustion and the oxygen to fuel ratio were varied.

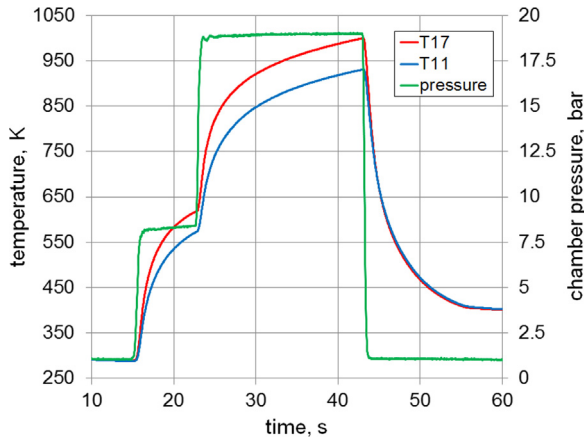


Fig. 2. Averaged temperature and pressure transients during Campaign C.

In the following sections the experimental setup is described at first. Then the load conditions and load phases are shown and discussed. In the next chapter the deformation and roughness development, the failure types, especially the doghouse effect, and the life-limiting mechanisms are shown and discussed. In the end the performance of the thermal barrier coatings is explained and a conclusion is given.

## 2. Lifetime experiment

### 2.1. Experimental setup

Five coaxial shear injectors in double-symmetric configuration are mounted in front of the combustion chamber. The oxygen posts have an inner diameter of 4 mm and a wall thickness of 0.5 mm. The outer methane gaps have a width of 0.5 mm. Details about the injector head assembly can be found in [7]. The cross section of the combustion chamber has a width of 48 mm and a height of 12 mm.

Fig. 1(a) shows a cut view of the fatigue segment and visualizes the fluid flows (red for hot-gas, blue for coolant). The fatigue segment includes a replaceable fatigue specimen made of the copper alloy CuCr1Zr. The specimen is attached with a floating bearing which allows free thermal expansion. It has 17 rectangular cooling channels with a height of 8 mm, a width of 2.5 mm, a rib thickness of 2 mm and a length of 96 mm. The wall thickness between the hot-gas exposed surface and the cooling channel bottom side is 1 mm. The specimen is loaded cyclically. After each cycle the deformation of the specimen's hot-gas wall is measured by a laser profile scanner. To inspect the hot-gas exposed surface without the need to disassemble the fatigue specimen, the water-cooled inspection plate on the opposite side is removed.

High pressure nitrogen at ambient temperature is used as coolant for the specimen. To ensure well defined conditions in the three central cooling channels the mass flow rates here are closed loop controlled individually (PID). The coolant supply for the remaining 14 channels are separated in two closed loop controlled lines. The mass flow rates in each of these five supply lines are measured by a Coriolis flow meter located downstream of the fatigue specimen. Also the inlet pressure is regulated by a PID-control. The temperature and pressure of the coolant are measured in the inlet and outlet manifolds of the three central and two additional cooling channels by thermocouples respectively pressure transducers (see Fig. 1(a)).

Furthermore, the specimen is equipped with several thermocouples in different positions and depths to measure the temperature distribution in the structure during each cycle. Fig. 1(b) shows the top view of the fatigue specimen with the green coordinate system in the center. In addition, the thermocouple positions T6-T23 (red for 3 mm and blue for 5 mm distance to the hot-gas exposed surface) are shown. The most central located thermocouple T9 has the coordinates  $x = -2.25$  mm/

$z = 1$  mm. The thermocouples have a spacing of 5 mm in axial (in hot-gas flow direction) and 4.5 mm in transversal (orthogonal to the hot-gas flow) direction respectively. They are located in the symmetry planes of the ribs and are pushed by spring constructions against the measurement locations in the eroded blind holes. The blue and red arrows indicate the flow directions of nitrogen (C) and hot-gas (HG). On the upper side of the fatigue specimen a thermocouple (PT100, coordinates:  $x = 11$  mm/  $z = 8$  mm) and a T-rosette strain gauge (coordinates:  $x = 34$  mm/  $z = 0$ ) are placed. The axial elongation is measured by an inductive displacement transducer. This transducer measures between two cantilevers with a distance of 37 mm, which are fixed with bolts on the upper side of the fatigue specimen. The positions of the contact points of the transducer are marked in Fig. 1(b) (coordinates:  $x = -35$  mm/  $z = 18.5$  mm respectively  $x = -35$  mm/  $z = -18.5$  mm).

In campaigns F and G metallic thermal barrier coatings were applied using high velocity oxyfuel spray (HVOF). This coating process stands for low porosity and low oxide content compared to other atmospheric spray processes [11,12]. Details of the coating process and the parameters can be found in [13]. The coating system consists of a 40  $\mu$ m thick NiCuCrAl bond-coat [14] and a 60  $\mu$ m thick top-coat made of the nickel-based superalloy 'Rene 80' [15]. After the spray process, the coating surface is ground and polished to achieve a roughness of  $Ra$  0.5  $\mu$ m. Campaign F was performed without any post-spray treatment, whereas the specimen for Campaign G was diffusion heat treated for six hours at 973 K in an argon atmosphere to enhance the coating adhesion and prevent the growth of delamination cracks between coating and substrate. The diffusion heat treatment also affects the micro structure of the entire specimen due to the long holding time at high temperatures (see Section 2.4.7).

### 2.2. Load conditions

A load cycle consists of three phases: pre-cooling, fire and post-cooling phase. For ignition reliability, controlled flame anchoring and combustion stability the fire phase consists of two different chamber pressure stages. Fig. 2 shows the chamber pressure and the temperature of thermocouples T11 and T17 averaged over all cycles of Campaign C. The position of the thermocouples can be found in Fig. 1(b). After start of the fire phase the pressure increases rapidly until an almost steady-state hot-gas status is reached (ignition stage). After 7.5 s the pressure increases and holds the nominal load for 20 s (nominal stage). In the post-cooling phase the combustion is stopped by closing the propellant supply and the chamber cools down. Both thermocouples respond to the thermal loads with rapidly increasing temperatures. T17 reaches higher temperatures and responds faster due to its smaller distance (3 mm) to the hot-gas exposed surface than T11 (5 mm).

As Fig. 2 indicates, the chamber pressure has a large impact on the thermal loading. After the widely used Bartz equation [16] following relationship between the heat transfer coefficient  $\alpha_{hg}$  and the chamber pressure  $p_{hg}$  applies:

$$\alpha_{hg} \propto p_{hg}^{0.8}. \quad (1)$$

Also the mixture ratio has a large effect. The stoichiometry of an oxygen/methane combustion is at a mixture ratio of 4. For mixture ratios close to this value the highest heat fluxes are reached.

Assuming a fully developed turbulent duct flow and a constant Prandtl number of 0.73 in the cooling channels, the following relationship between coolant mass flow and heat transfer coefficient  $\alpha_c$  can be derived from [17]:

$$\alpha_c \propto \frac{(\zeta/8)Re}{1 - 2.404\sqrt{\zeta/8}}, \quad (2)$$

with  $\zeta = (1.8\log_{10}Re - 1.5)^{-2}$  and the Reynolds number  $Re$ , which is proportional to the mass flow  $\dot{m}_c$ . For high Reynolds numbers (as present in the cooling channels) the relationship can be simplified to:

**Table 1**  
Load conditions in campaigns B-K.

Campaign	mixture ratio		chamber pressure		maximum temperature (T17)		cycles
	mean	standard deviation	mean	standard deviation	mean	standard deviation	
B	3.87	0.16	17.2 bar	0.5 bar	929 K	36.6 K	45
C	3.92	0.07	19.0 bar	0.4 bar	998 K	12.8 K	48
D	3.94	0.05	19.2 bar	0.3 bar	973 K	24.9 K	46
E	3.87	0.07	19.1 bar	0.3 bar	1020 K	10.5 K	16
F	3.65	/	19.3 bar	/	983 K	/	1
G	3.89	0.04	19.3 bar	0.2 bar	975 K	16.9 K	36
H	3.88	0.05	28.8 bar	0.2 bar	1017 K	13.0 K	15
I	3.95	/	28.7 bar	/	976* K	/	2
J	3.42	0.04	28.7 bar	0.2 bar	943 K	5.6 K	34
K	3.41	0.03	28.5 bar	0.1 bar	976 K	17.1 K	24

\*Due to a manufacturing error this value was measured 4.5 mm instead of 3 mm apart from the hot-gas exposed surface.

$$\alpha_c \propto \dot{m}_c \tag{3}$$

For a detailed discussion of the effects of chamber pressure, mixture ratio and coolant mass flow on the temperatures see [7].

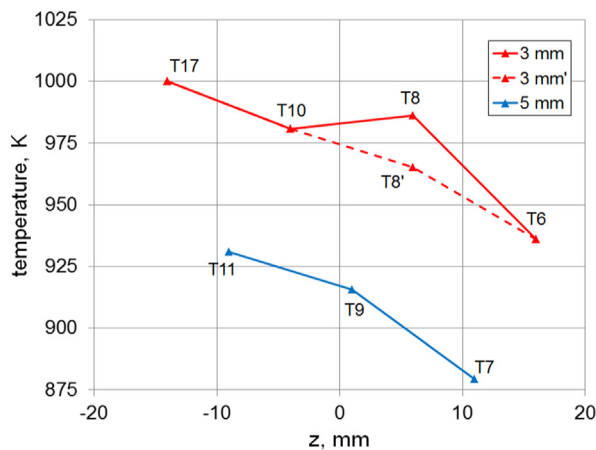
Table 1 shows a comparison of the campaigns B-K in terms of mean values and standard deviations of mixture ratio, chamber pressure and maximum temperature of Thermocouple T17. In addition, the number of cycles is shown. Campaigns B-G are executed under identical coolant conditions. The coolant pressure is 70 bar and the mass flow per channel is 8 g/s. In campaigns H-K the coolant pressure and mass flow are increased to 80 bar and 12 g/s.

The initial low pressure stage lasts 7.5 s for all tests. The subsequent high pressure stage lasts 20 s for campaigns B-G and K and 10 s for campaigns H-J. The load conditions according to Table 1 show the values of the nominal stages. The ignition stages have approximately the same mixture ratios and half the chamber pressures. The duration of the post-cooling phase is controlled manually, but not stopped before the temperature in the specimen has fallen below 400 K.

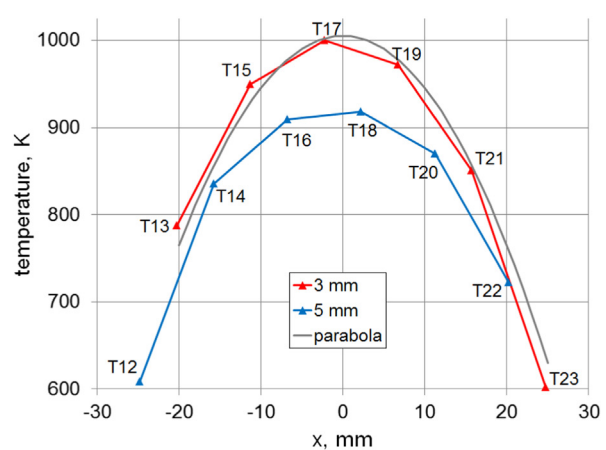
Fig. 3 shows the temperature distribution in the specimen at the end of the second stage averaged over all cycles of Campaign C. The temperature distribution is qualitatively representative for all test campaigns. The temperature is decreasing in hot-gas flow direction (z-direction). This is mainly caused by the strong cooling effect of the impinging nitrogen in the cooling channel inlet region (at z = 44 mm). In addition the nitrogen temperature is increasing in its flow direction (negative z-direction). The thermal boundary layer of the hot-gas is increasing in z-direction, which reduces local heat fluxes. The axial temperature gradient between T6 and T17 is approximately 2.4 K/mm.

The vertical temperature gradient at a distance of 3 mm (red curves) to 5 mm (blue curve) to the hot-gas exposed surface amounts to roughly 30 K/mm. Assuming this gradient to be constant, the extrapolated temperature of T17 reaches 1090 K at the surface exposed to the hot-gas. Thermocouple T8 reports higher temperatures than expected. This is due to a manufacturing error, causing T8 to be positioned at just 2.3 mm instead of the nominal distance of 3 mm to the hot-gas exposed surface. Applying said temperature gradient of 30 K/mm, the measured temperature is 21 K too high. T8' indicates the temperature corrected by this value, which seems realistic. The depths of the remaining thermocouples are inside the manufacturing tolerance of +/- 0.2 mm, which results in a +/- 6 K uncertainty. The thermocouples have a measuring tolerance less than 4 K at 1000 K and a response time less than 0.15 s.

The transverse temperature distribution (Fig. 3(b)) decreases away from the symmetry axis, since the hot-gas velocity and temperature are decreased in the corner regions of the chamber. This again leads to a decreased heat flux and therefore reduced wall temperatures in those regions. Furthermore, the three outermost cooling channels on both sides overhang the hot-gas cross section. The temperature profile at a distance of 3 mm to the hot-gas exposed surface can be approximated with a parabola of equation  $T(x) = -0.6x^2 \cdot K/m^2 + 1005K$ . A comparison of the thermocouple measurements with the (symmetric) parabola shows a slight asymmetry. The asymmetric temperature distribution causes an asymmetric deformation profile, as shown in Fig. 6(a). The temperature distribution at the hot-gas walls upstream of the fatigue segment is verified to be asymmetric as well. Therefore, it is concluded that this is caused by the hot-gas flow, possibly by a non-uniform fuel



(a) Thermocouples in axial direction



(b) Thermocouples in transversal direction

**Fig. 3.** Averaged temperature distribution at the extinction time point for Campaign C.

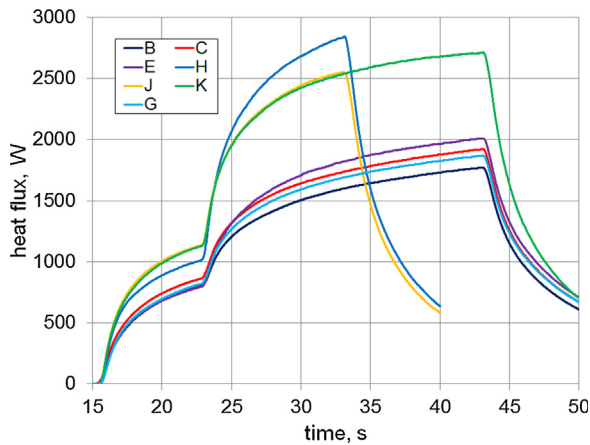


Fig. 4. Averaged integral heat flux transients of the central cooling channel for selected test campaigns.

distribution to the five injectors.

Fig. 4 shows the averaged integral heat flux transients of the central cooling channel during campaigns B-K. The heat flux is calculated by the product of the specific heat capacity, the mass flow and the difference of the inlet to the outlet temperatures of the nitrogen. The change of enthalpy due to change of pressure is neglected, since the pressure drop in the cooling channels is merely around 0.1 bar. When a steady-state behavior is reached, the calculated cooling channel heat flux corresponds nearly to the heat flux over one rib and one cooling channel width in the center of the hot-gas exposed surface of the specimen. The nitrogen temperatures are measured at the manifolds. The thermocouples as well as their positions remain the same in every test campaign, as the manifolds are not replaced after each of the test campaigns. The position and the contact of the thermocouples in the specimen depend on manufacturing accuracy. Because of the extremely high temperature gradients in space as well as time, small differences can cause large errors. Therefore, the nitrogen temperatures are rather to be used for relative comparison of test campaigns in terms of the thermal loading.

At the end of the fire phase, the heat flux into the central cooling channel averages to 1922 W in Campaign C. Assuming steady-state behavior, this corresponds to a heat flux density at the hot-gas side of  $4.27 \text{ MW/m}^2$ . In Campaign B this value is 7.9% less, caused by the 9.5% lower chamber pressure and a slightly lower mixture ratio. In Campaign E, the increased surface roughness causes a 4.5% higher heat flux despite a slightly lower mixture ratio. The thermal barrier coating in Campaign G reduces the heat flux by 2.8%. The 50% higher chamber pressure, the much lower mixture ratio and increased roughness in Campaign K result in a 41.1% increase of heat flux. The almost identical heat flux curves of campaigns J and K along the entire first 17.5 s of operation indicate an excellent repeatability of the thermal loads. The maximum heat flux of the central cooling channel in Campaign H is 11.4% higher than in Campaign J, caused by the higher mixture ratio.

### 2.3. Load phases

The hot-gas wall of the specimen has to resist three load phases during a load cycle. These load phases are marked in Fig. 5 and described below:

1. Ignition and stage change (during  $15 \text{ s} < \text{time} < 17.6 \text{ s}$  and  $23 \text{ s} < \text{time} < 24.2 \text{ s}$ ): After ignition respectively stage change the temperature of the hot-gas wall increases rapidly which thus expands. The rest of the structure is still cold and restrains this expansion. As a result, the hot-gas exposed surface bends convexly while the upper side of the specimen bends concavely, which

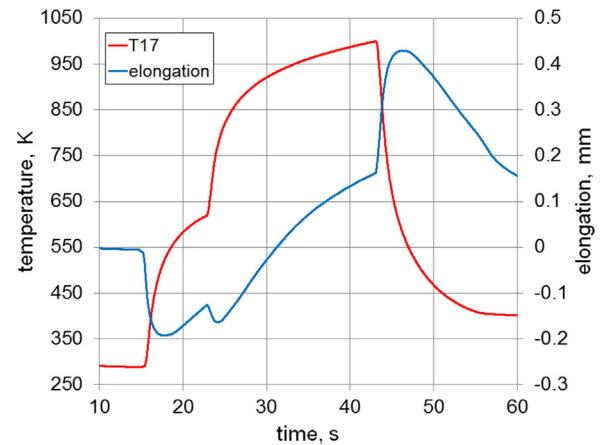


Fig. 5. Averaged temperature and elongation transients during Campaign C.

decreases the distance between both measurement cantilevers of the displacement transducer, as shown in Fig. 5. Very high in-plane compression stresses are induced into the hot-gas wall due to the thermal loading. In addition, the walls between coolant and hot-gas bulge into the hot-gas due to the large pressure difference. In combination with high temperatures and time, this leads to creeping. Due to the short duration and low temperatures in comparison to the other phases creeping can though be neglected in phase 1.

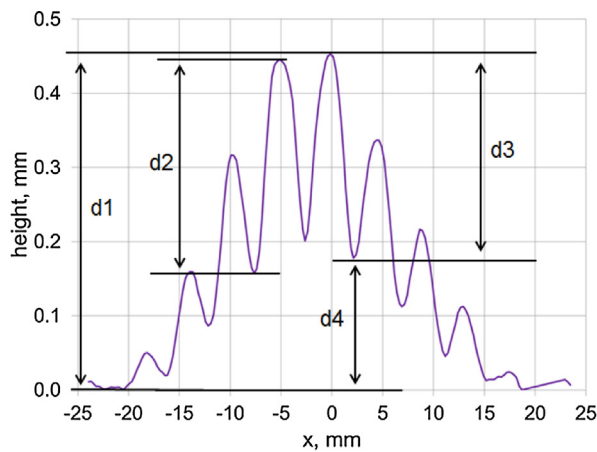
2. Hot phase (during  $17.6 \text{ s} < \text{time} < 23 \text{ s}$  and  $24.2 \text{ s} < \text{time} < 43 \text{ s}$ ): Afterwards, the heat reaches the back parts of the structure and the thermally induced stresses decrease, until a steady-state is reached (not reached in the tests). As the specimen is actively cooled, the in-plane compression stresses in the hot-gas wall however would not reach zero. The bending now decreases, as the entire specimen expands thermally. Therefore, the measured elongation increases (see Fig. 5). In contrast to phase 1 and 3 creeping is important, since the thin hot-gas wall has to resist the pressure differences between hot-gas and coolant as well as compressive stresses due to the temperature differences (see above) during a comparatively long duration, while exceeding temperatures of 1000 K. Additionally, blanching, abrasion and thermal aging can be present in this phase.
3. Shutdown phase (during  $43 \text{ s} < \text{time} < 46 \text{ s}$ ): After shutdown the temperature of the hot-gas wall decreases much faster than the rest of the structure due to the low heat capacity of the thin wall as well as the high heat flux to the impinging coolant. This leads to very high in-plane tensile stresses and a concave bending of the hot-gas exposed surface, which rapidly increases the measured elongation on the upper side (see Fig. 5). Because of the change in load direction a Bauschinger effect [18] occurrence must be assumed, which decreases the tensile yield strength. In this phase creeping can again be neglected, due to quickly decreasing temperatures. After 46 s, the measured elongation decreases. This indicates that the vertical temperature difference decreases, which in turn reduces the bending of the specimen and in-plane tensile stresses. As the temperatures fall below 600 K, the yield strength is increased. In conclusion the loading after 46 s can be neglected.

### 2.4. Deformations and lifetime

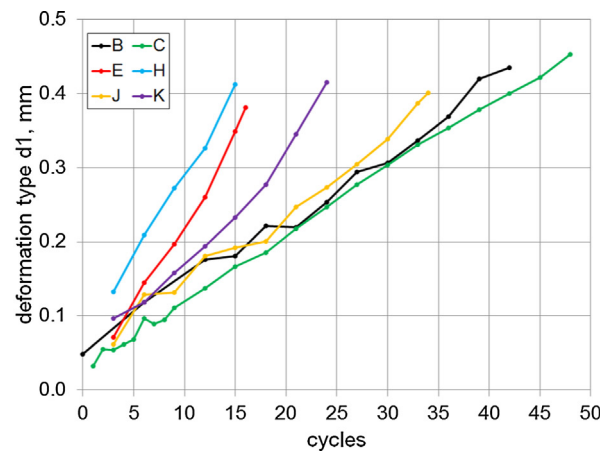
Table 2 shows the initial mean roughness  $R_a$  on the hot-gas exposed surface and the presence of thermal barrier coatings on the specimen. Furthermore it is shown, whether and why the specimen failed. The height of four different types of deformation measures at the end of each test campaign and their average changes per cycle are listed accordingly.

**Table 2**  
Initial and deformation properties of the specimen in campaigns B-K.

Campaign	initial mean roughness	special feature	failure type	final deformation, $\mu\text{m}$				average slope, $\mu\text{m}/\text{cycle}$	
				d1	d2	d3	d4	d1	d2
B	$< 0.5\mu\text{m}$	/	/	46	30	29	16	1.02	0.67
C	$< 0.5\mu\text{m}$	/	'doghouse'	45	29	28	18	0.94	0.60
D	$< 0.5\mu\text{m}$	/	weld seam fracture	45	25	24	21	0.98	0.54
E	$4\mu\text{m}$	/	'doghouse'	38	27	27	11	2.38	1.69
F	$< 0.5\mu\text{m}$	TBC	TBC delamination	/	/	/	/	/	/
G	$< 0.5\mu\text{m}$	TBC	weld seam fracture	45	33	33	12	1.25	0.92
H	$2\mu\text{m}$	/	'doghouse'	41	26	26	15	2.73	1.73
I	$2\mu\text{m}$	/	melting	/	/	/	/	/	/
J	$2\mu\text{m}$	/	'doghouse'	40	27	27	13	1.18	0.79
K	$2\mu\text{m}$	/	/	41	26	25	17	1.71	1.08



(a) Deformation type definition



(b) Deformation type d1 development

**Fig. 6.** Deformation measurement.

Each underlying deformation profile is measured 20 mm downstream from the leading edge of the specimen using a laser-profile-scanner in transverse direction. The deformation measures are defined in Fig. 6(a), where the measured profile at the end of Campaign C is shown. Deformation type d1 is the difference of the global maximum and global minimum. Deformation type d2 is the overall greatest difference of a local maximum and a neighboring local minimum. Deformation type d3 is the greatest difference of the global maximum and a neighboring local minimum. Deformation type d4 is the difference of type d1 and d3. Neighboring means a distance smaller than 4.5 mm (one channel plus one rib width).

**2.4.1. Deformation development**

Despite different load conditions, the doghouse effect occurs reproducibly, when a deformation type d1 height of around  $40\mu\text{m}$  is reached. For test campaigns with low loading (B, C, D, G) the critical value is slightly higher (approximately  $45\mu\text{m}$ ). The critical deformations of types d2 and d3 are roughly  $30\mu\text{m}$ . The average slope of deformation is increasing with temperature gradient and level.

Fig. 6(b) shows the development of the type d1 deformation during campaigns B, C, E, H, J and K. It is shown that the deformations are increasing almost linearly with the number of cycles in all test campaigns.

**2.4.2. Doghouse effect**

In campaigns C, E, H and J the so called doghouse effect occurred. After detection during leakage test (at least every 3rd cycle or if suspected) the test campaigns were ended.

Fig. 7 shows the hot-gas exposed surface of the fatigue specimen

after 48 cycles (1320 s of fire phase in total) in Campaign C. Two cracks are visible at the wall of the central cooling channel. To investigate these cracks, the fatigue specimen has been cut at the crack tip. Fig. 8 shows the cut views A-A and B-B (marked in Fig. 7) through the five central cooling channels. Due to material removal by the utilized saw blade and the metallographic preparation, both cut views differ slightly in their axial positions. In cut view A-A the cooling channel wall has already failed, whereas the crack in cut view B-B has not yet reached the hot-gas exposed surface. Both cracks are shown in Fig. 9 in detail. The original shape of the cooling channel and the micro structure is shown as overlay in Fig. 9(a). The strong plastic deformation of the micro structure indicates necking caused by tensile loads.

Fig. 10 shows the 'doghouse' failure and micro structure in the central cooling channel wall in Campaign E. In comparison to Campaign C the material has had a larger initial grain size. Along the hot-gas exposed surface the material has strongly degraded due to sand-blasting in provocation of the higher initial surface roughness. The leakage due to the 'doghouse' failure (in cold state) and the crack length are extremely small in Campaign E. Therefore it can be concluded that this 'doghouse' failure occurred very shortly before the campaign was ended. The 'doghouse' shape is not symmetrical, which is a consequence of the non-uniform grain size distribution.

Fig. 11 shows the 'doghouse' failure in the central cooling channel wall and its micro structure in Campaign H. The initial grain size is very large. The effect of the grain size on the lifetime is still not clear and will be investigated in the future. On one hand, large grains reduce creeping, since that effect occurs predominantly on the grain boundaries and larger grains lead to less thereof. On the other hand, large grains increase the appearance of yielding, since it occurs through

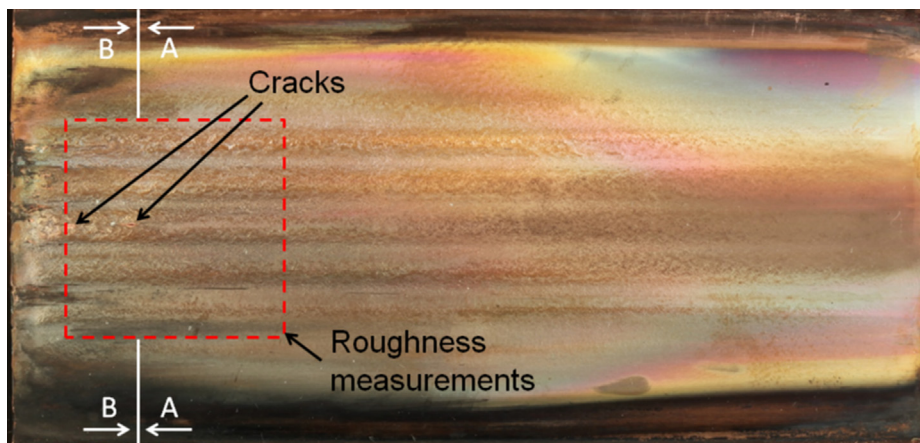


Fig. 7. hot-gas exposed surface after 48 cycles (Campaign C).



Fig. 8. Cut views after 48 cycles (Campaign C).

dislocation motion and grain boundaries mitigate such motion.

Fig. 12 shows the 'doghouse' failure in the central cooling channel wall and the surrounding micro structure in Campaign J. The initial grain size is comparable to that in Campaign C. In contrast to campaigns E and H the roof of the 'doghouse' is very straight and symmetric, due to its small grain size and very uniform grain distribution.

#### 2.4.3. Other failures

Due to leakage of a weld seam, campaigns D and G had to be stopped before the doghouse effect occurred. Due to manufacturing constraints, the electron-beam welding is necessary to close the wire eroded cooling channels in axial direction with two caps. The welding process was improved following Campaign G in order to lower the

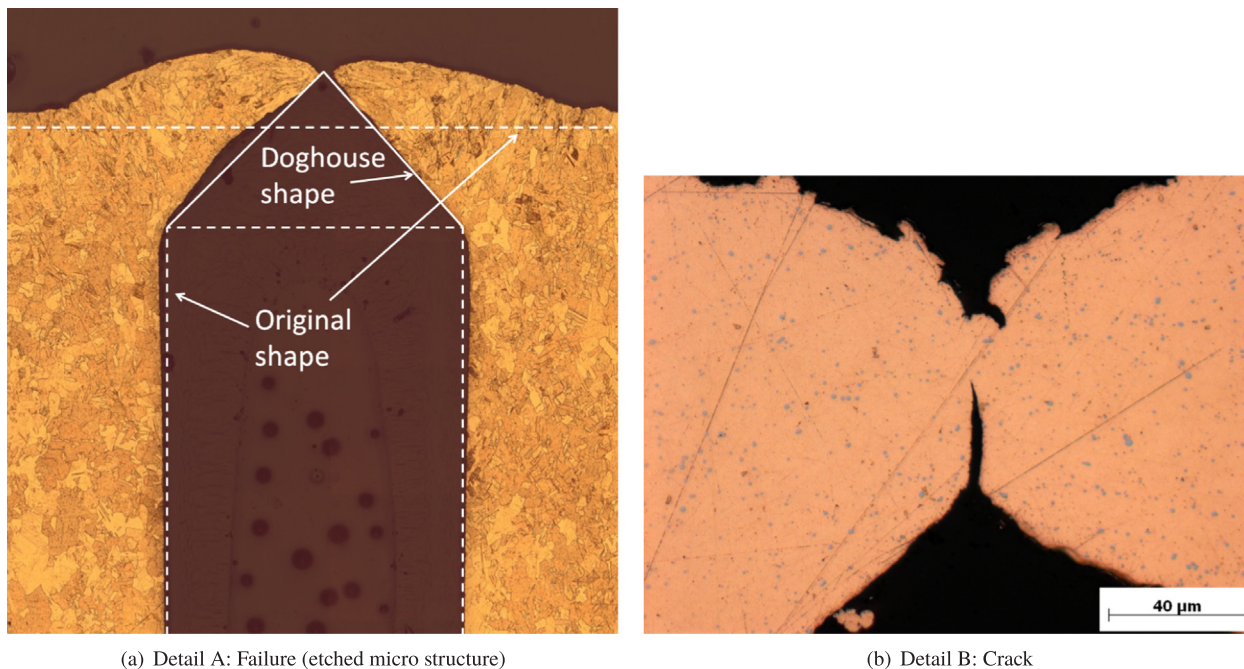


Fig. 9. Cut view details after 48 cycles (Campaign C).



Fig. 10. 'Doghouse' failure in Campaign E (etched micro structure).

probability of weld seam failure.

In Campaign F the thermal barrier coating failed due to delamination already during the first load cycle. This is discussed in Section 2.5.

In Campaign I the hot-gas wall melted during the second load cycle in a large area (see Fig. 13). During the main stage of the second cycle the integral wall heat flux of the central cooling channel was 7% higher than in all other tests and 11% higher than in the first cycle of Campaign I. The mixture ratio (3.96) and pressure (28.8) were almost the same as during the first cycle (3.93 respectively 28.6). No manufacturing error could be detected in the remaining material. Therefore, it is assumed that a combustion instability has increased the heat flux significantly and that a critical wall temperature has been reached, which caused a rupture due to the pressure difference between coolant and hot-gas. The fact that the material failed during the fire phase and not during the post-cooling phase supports the hypothesis that the failure was caused by pressure rupture and not by fatigue. It is assumed that a massive leakage in one cooling channel has reduced the drag of this coolant line. This would decrease the coolant's mass flow of the other cooling channels and would therefore increase the wall temperature of other parts of the specimen towards the critical temperature.

Campaigns B and K were ended, before any failure occurred. It is assumed that campaigns B, D, G and K are close to a 'doghouse' failure,

since their deformation type d1 values are close to the critical value.

#### 2.4.4. Blanching and combustion instabilities

A cyclic oxidation and reduction of the copper causes blanching (see [19,20] for details). The resulting surface layer whitens and starts to flake off. Blanching in combination with abrasion increases the surface roughness (see Section 2.4.5) and reduces the hot-gas wall thickness (see Section 2.4.8). Strong blanching occurred in Campaign B due to combustion instabilities. During a combustion instability, the local species concentration varies strongly. This leads to an alternation of an oxidizing and deoxidizing environment. Combustion instabilities can be detected by measuring the acoustic spectrum with high frequency pressure sensors and comparing it to a reference spectrum from a stable test, as shown in [7]. Furthermore, combustion instabilities can increase the wall heat flux, especially in the near-injector region, but also on the fatigue specimen (see [7]). It is assumed that the combustion instabilities which occurred during Campaign B were caused by a failed flame anchoring on the injector elements. Combustion instabilities could be prevented in almost all subsequent tests by an improved ignition process using short sequences of additional oxygen during the ignition and stage change phase.

The average slope of deformation in Campaign B is slightly higher than in Campaign C (see Table 2), although the nominal loading is

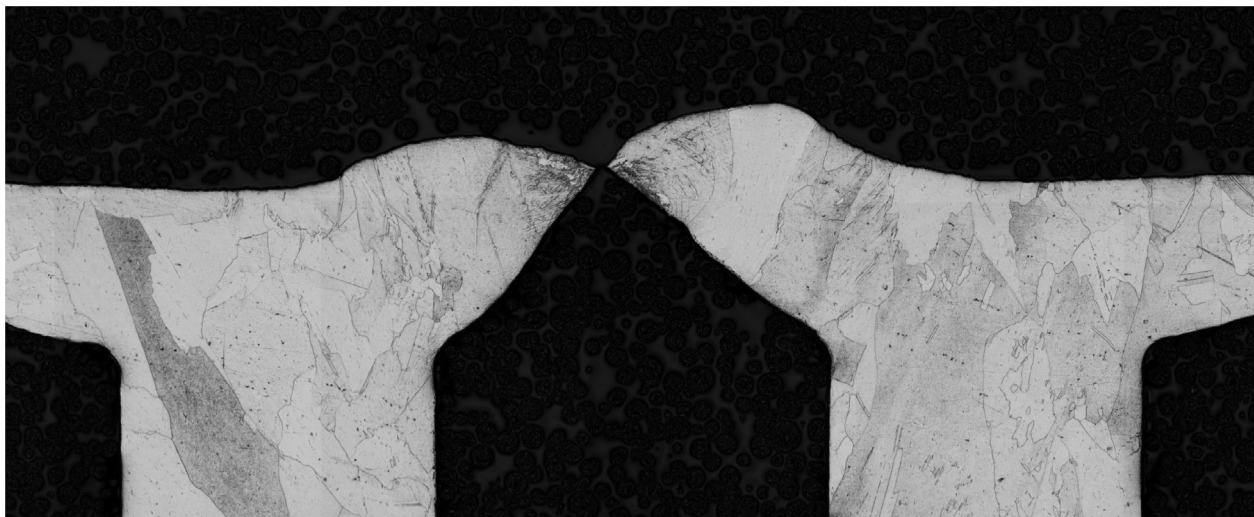


Fig. 11. 'Doghouse' failure in Campaign H (etched micro structure).

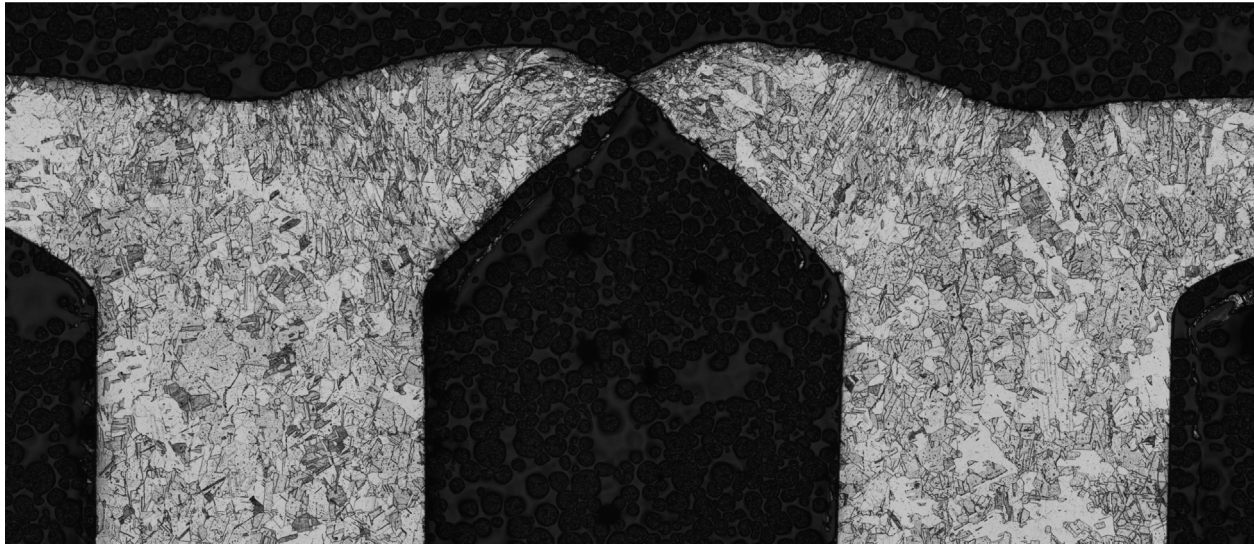


Fig. 12. 'Doghhouse' failure in Campaign J (etched micro structure).



Fig. 13. Melted hot-gas wall in Campaign I.

lower due to the lower chamber pressure (see Table 1). Therefore, it can be concluded that combustion instabilities reduce the lifetime significantly. Strong combustion instabilities occurred during tests B2 (second cycle in Campaign B), B4, B7, B22 and B30, as shown in [7]. No direct response of the deformation height on the unstable tests is identifiable in Fig. 6(b). Therefore, it is assumed that unstable tests affect the lifetime mainly due to the initiation of blanching, which increases the roughness and with it also the wall heat flux in the subsequent tests. The failure in Campaign I (see Section 2.4.3 shows that an increase of the wall heat flux during a combustion instability can cause a rupture due to an exceeding of the critical wall temperature.

2.4.5. Surface roughness

The mean roughness  $R_a$  is defined as follows:

$$R_a = \frac{1}{M} \sum_{m=1}^M \left| y(x_m, z_m) - \frac{1}{M} \sum_{m=1}^M y(x_m, z_m) \right| \quad (4)$$

$R_a$  is measured along lines in flow direction ( $0^\circ$ ) and transverse to it ( $90^\circ$ ), both at nine different locations in the red dotted quad in Fig. 7. This quad is subdivided in nine equal quads, and the measurements are performed in the centers of these quads along 4 mm long tracks.

Fig. 14 shows the roughness development on the hot-gas exposed surface of the specimen during campaigns B and C. The values of both measurement directions are averaged over the nine measurement locations. The initial roughness before the first hot-gas test is  $R_a = 0.5 \mu\text{m}$

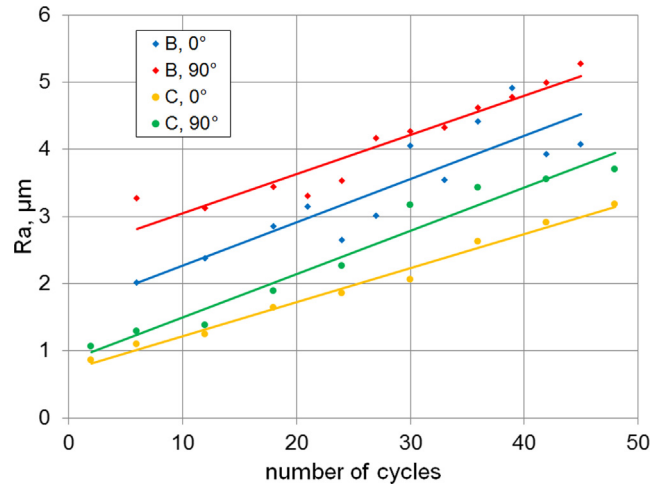


Fig. 14. Roughness development.

in campaigns B and C (see Table 2). In Campaign C the roughness increases nearly linearly. In Campaign B the roughness increase during the first six cycles is much higher than in Campaign C. The further roughness development is much more erratic than in Campaign C. It is assumed that the combustion instabilities are the reason for that. Possibly, the instabilities during tests B2 and B4 are the reason for the much higher roughness after Test B6 in comparison to the roughness after Test C6. After that, the roughness in  $90^\circ$  direction decreases slightly in Campaign B until Test B12. This could be caused by flaking off of the reacted layers. During the tests B28-B30, a strong roughness increase in  $0^\circ$  direction is detectable, possibly caused by the instabilities in Test B30. After this, the roughness in  $0^\circ$  direction decreases until Test B33. It could be caused by flaking off of the reacted layers again.

It is still unclear, which effect causes the roughness increase in tests without apparent blanching in macroscale, like in Campaign C. It could be caused by microscale blanching, plastic deformation, thermal aging or abrasion. Plastic deformation can increase the roughness due to non-uniform deformation of the grains. Thermal aging can increase the roughness due to non-uniform grain growth or chromium precipitates. Abrasion can increase the roughness due to partial damage of the hot-gas exposed surface.

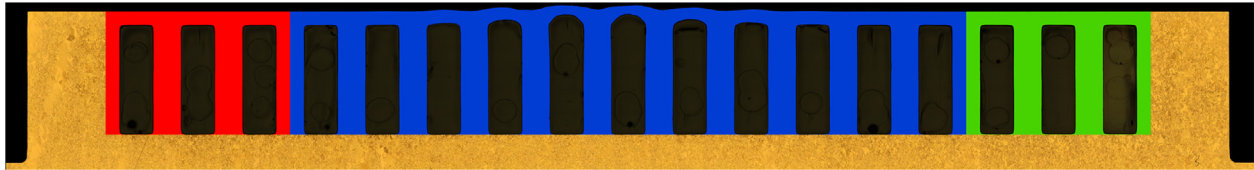


Fig. 15. Optical abrasion study.

#### 2.4.6. Yielding and creeping

The effect of phase 1 on the lifetime in campaigns J and K can be assumed as equal due to very similar test conditions during the first 17.5 s. Furthermore, the results of Campaign A [7] have shown that below a wall temperature of 850 K and in the relevant time scales no residual deformations occur. Therefore, (relevant) creeping occurs only during the nominal hot-gas stage. In Campaign K the duration of the nominal hot-gas stage is doubled in comparison to Campaign J and higher wall temperatures are reached. Therefore, creeping per cycle should be increased by more than a factor of 2. But the slope of deformation is only increased by around 40%. Therefore it is hypothesized that the effect of creeping on the lifetime at least in Campaign J is relatively small and the lifetime is mostly affected by the shutdown phase.

A comparison of campaigns C and E shows that the higher initial roughness in Campaign E decreases the lifetime by a factor of 3. The higher roughness increases the heat flux as shown in Fig. 4. This increases the wall temperatures, the vertical temperature gradients and the temperature of the upper side of the specimen. The roughness is increasing with the number of load cycles in the central part of the hot-gas exposed surface (see Fig. 14). This reduces the differences between campaigns C and E in the central region. The roughness in the outer regions of the hot-gas exposed surface is increasing much slower. Therefore, the difference of the wall heat flux between Campaigns C and E remains large in these regions. This increases the upper side temperature of the specimen significantly. A higher upper side temperature increases the loading of the shutdown phase due to stronger thermal induced bending. If the effect of roughness on the central hot-gas exposed surface would be more important than its effect on the outer hot-gas exposed surface, a change of the deformation slope should be detectable, which is not the case. Therefore it is assumed that the higher initial roughness mostly affects the lifetime through the shutdown phase. Still unclear is the effect of the degraded micro structure due to the sand blasting in Campaign E.

In the lifetime studies of cooling channel structures under thermo-mechanical loading in [6] the thermomechanical fatigue (TMF) panel made of CuCr1Zr was heated by a laser with up to 20 MW/m<sup>2</sup>. The TMF panel withstood 93 cycles with surface temperatures of about 900 K and 81 cycles with 750 K until its failure. In each cycle the laser power was ramped up over 2 s, held for 598 s and ramped down over 9 s. The total laser-on holding time was 104052 s. The total duration of the nominal load stage in Campaign C is 960 s until the specimen failed in 'doghouse' mode. Although the heat fluxes of these laser tests were higher than in the hot-gas tests in the present work, the lifetime was larger by a factor > 100. One reason of this longer durability is the lower surface temperature of the laser tests. A second reason could be the slow reduction of the laser power, which significantly reduces the tensile stresses in the hot-gas wall during the post-cooling phase. This would support the hypothesis that the yielding during the post-cooling phase is very important for the lifetime. In addition, the cut view of the failed TMF panel in [6] does not show a typical 'doghouse' shape: the crack did not grow in the center of the hot-gas wall and no necking was visible. This could be caused by the reduced tensile stresses during the post-cooling phase due to the laser power ramping down.

#### 2.4.7. Thermal aging

A material which is exposed to high temperatures over time changes

its micro structure. This degradation is called thermal aging. For CuCr1Zr it is expected that it decreases the strength strongly and increases the ductility slightly (see [21] for details).

A comparison of the grain size distribution and the chromium precipitates of the central cooling channel walls (which reach more than 1000 K during the tests) with those of the outer cooling channel walls (which does not reach more than 600 K during the tests) after each test campaign shows no significant differences. Therefore, it is concluded that the effect of thermal aging is negligible for during the short lifetime of the samples.

#### 2.4.8. Abrasion

The abrasion after Campaign B is investigated optically. The cut view of the highest deformed region is used for this study (see Fig. 15). The lateral and upper cooling channel walls are separated in three regions and are colored differently. The red and green colored regions represent the initial geometry, since they are overhanging the hot-gas exposed zone and no residual deformation could be detected. The blue colored region is inside of the hot-gas exposed zone. If abrasion would be relevant, the area per channel of the blue region (measured by the number of pixels) should be smaller than in the other regions. Yielding and creeping in plane direction should not affect the area, since the lateral and lower boundaries of the blue region are in a zone, which is not deformed during the test campaign in a relevant magnitude. It is assumed that yielding and creeping in normal direction (nearly plane strain condition) and the density change through oxidation can be neglected.

The area per channel for the red and green region is 20.01 mm<sup>2</sup> and for the blue region 20.03 mm<sup>2</sup>. Taking the measurement accuracy (estimated as  $\pm 0.1$  mm<sup>2</sup>) into account no change of the area per channel could be detected. Campaign B was chosen for this study, since it is the only test campaign, where strong blanching occurred, which increases the abrasion. Therefore it is concluded that abrasion can be neglected for this kind of lifetime studies.

### 2.5. Thermal barrier coatings

#### 2.5.1. Campaign F: TBC as sprayed

In Campaign F (coating without diffusion heat treatment), the coating delaminated during the heating phase of the first cycle. It has been shown recently [10] that small thermally grown cracks at the substrate/coating interface may lead to a delamination and buckling of the coating. In laser-induced thermal cycling experiments without hot-gas flow, this failure lead to small blisters on the coating surface with diameters less than 5 mm. It is assumed that additional mechanical loads (e.g. wall shear stresses) during the fire phase led to a rapid growth of the small delamination cracks and a total loss of the coating.

#### 2.5.2. Campaign G: TBC diffusion heat treated

A diffusion heat treatment enhances the adhesion strength of the coating and reduces the growth of delamination cracks. It is supposed that, if the delamination crack growth is hindered by this diffusion heat treatment, no buckling or large-scale delamination can be expected in the coatings [10]. After Campaign G, the diffusion heat treated coating showed neither buckling nor delamination even after 36 cycles, although a network of vertical (relating to the coating surface) cracks has formed in the entire coating (see Fig. 16). The mechanism of this crack

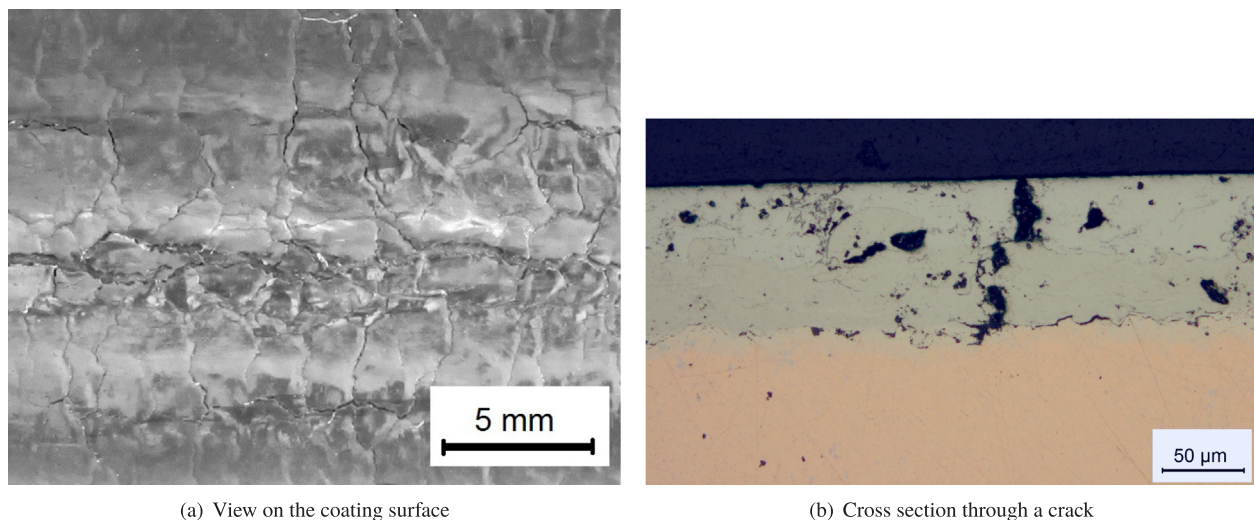


Fig. 16. Crack network in the coating after 36 test cycles (Campaign G).

growth has been elucidated in detail in previous work [10]: At high temperature, the thermal expansion of the hot coating surface is constrained by the cooled copper substrate. This results in compressive strains that exceed the yield strength. Plastic deformation leads to a reduction of the elastic component of the strain, so that subsequent cooling generates large tensile strains, and the coatings may crack [10,22]. Cyclic loading leads to further crack growth, so that small cracks grow together and form a crack network, as observed after the 36 cycles of this test campaign.

Since the coating was still adhering to the copper substrate, it is supposed that these cracks can be tolerated in rocket engine applications. Furthermore, the larger heat flux in full-scale engines causes a larger temperature gradient in the coating that will lead to less thermal strains in the near-substrate part of the coating (see [10] for a more detailed discussion). Thus, cracks may stop upon reaching the substrate. But the exact mechanism of the propagation of vertical cracks, especially under cyclic loading, is not fully understood yet, and future work will focus on this crack propagation.

The coating system was designed for rocket engine applications with wall heat flux densities in the order of magnitude of  $100 \text{ MW/m}^2$ . In Campaign G, heat flux densities of about  $4.2 \text{ MW/m}^2$  are reached (see Section 2.2), so that the thermal insulation effect by the thin metallic coating is not significant. As shown in Fig. 4, the heat flux in the central cooling channel is only slightly reduced when a coating is applied. This results in a deformed cooling channel structure similar to the uncoated state (see Fig. 17)). Furthermore,  $100 \mu\text{m}$  of the copper wall had to be removed before coating application to fit the coated sample in the available space in the test bed. This increased the weakness of the cooling channel structure.

### 3. Conclusion

In this paper the setup of a lifetime experiment for rocket combustion chamber structures with an actively cooled, replaceable and cyclically loaded fatigue specimen made of CuCr1Zr is described. The transient, thermal field of the specimen is explained exemplarily. It is

shown that an increasing mixture ratio, chamber pressure and surface roughness increase the wall heat flux.

During one load cycle, the hot-gas wall of the specimen has to resist three different load phases. The first load phase is dominated by in-plane compression stresses. During the second load phase the compression stresses decrease and the pressure difference between hot-gas and coolant becomes dominant. In the third load phase the loading shifts abruptly into tensile stress. It is assumed that the third load phase is most important for the lifetime.

The vertical deformation of the hot-gas wall above the cooling channels increases almost linearly with the number of cycles. A critical value for the vertical deformation is found which indicate a 'doghouse' failure. In total eleven test campaigns were performed, thereof four ended with clear 'doghouse' failures. The 'doghouse' failures are characterized analyzing the micro structure at the cuts through the failed cooling channels.

Five life-limiting effects, namely creeping, yielding, blanching, thermal aging and abrasion are discussed. It can be concluded that thermal aging and abrasion can be neglected for these experiments. In addition, it can be concluded that the wall thickness removal by combined blanching and abrasion can be neglected. More important is the roughness increase by blanching, which increases the wall heat flux and thereby the thermal loading. It is concluded that yielding, mostly caused by tensile stresses during the third load phase, is the dominant life-limiting effect. The effect of creeping is presumably small, due to the short total duration of load. If a critical temperature is exceeded, the wall fails by rupture due to the reduced material strength and the pressure difference between coolant and hot-gas.

In addition, tests with thermal barrier coatings (TBCs) were performed. It is shown that they can decrease the wall heat flux slightly. A TBC, which was not diffusion heat treated, delaminated during the first load cycle. A diffusion heat treated TBC could resist the hot-gas for 36 cycles, but the resulting deformations were stronger than in the specimens without TBC due to a smaller CuCr1Zr wall thickness.

In the future the authors are planning to investigate the reproducibility of the experiment and the effect of the micro structure. In



Fig. 17. Deformed shape of the central cooling channel structure of the coated specimen after 36 cycles, cross-sectional view.

addition the authors are planning to decrease the oxygen and fuel feeding slowly after end of the nominal stage to prove the hypothesis that the third load stage is dominant for the lifetime.

### Declaration of Competing Interest

None.

### Acknowledgments

Financial support has been provided by the German Research Foundation (Deutsche Forschungsgemeinschaft – DFG) in the framework of the Sonderforschungsbereich Transregio 40.

### References

- [1] Quentmeyer R. Experimental fatigue life investigation of cylindrical thrust chambers. In: 13th AIAA/SAE propulsion conference, NASA-TM-X-73665; July 1977. <https://doi.org/10.2514/6.1977-893>.
- [2] Jankovsky R, Arya V, Kazaroff J, Halford G. Structurally compliant rocket engine combustion chamber— experimental and analytical validation. *J Spacecr Rock* 1995;32(4):645–52. <https://doi.org/10.2514/3.26665>.
- [3] Pavli A, Kazaroff J, Jankovsky R. Hot fire fatigue testing results for the compliant combustion chamber, NASA TP 3223; 1992.
- [4] Anderson W, Sisco J, Sung I. Rocket combustor experiments and analyses. In: 14th Annual thermal and fluids analysis workshop [CD-ROM], NASA Langley Research Center, Hampton, VA; Aug. 2003.
- [5] Kimura T, Hashimoto T, Sato M, Takada S, Moriya S, Yagishita T, et al. Firing tests and lifetime analysis of combustion chamber. *J Propul Power* 2016;32(5):1087–94. <https://doi.org/10.2514/1.B35973>.
- [6] Thiede R, Riccius J, Reese S. Life prediction of rocket combustion-chamber-type thermomechanical fatigue panels. *J Propul Power* 2017;33(6):1529–42. <https://doi.org/10.2514/1.B36361>.
- [7] Hötte F, Lungu P, von Sethe C, Fiedler T, Haupt M, Haidn O. Experimental investigations of thermo-mechanical fluid-structure interaction in rocket combustion chambers. *J Propul Power* 2019;35(5):906–16. <https://doi.org/10.2514/1.B37439>.
- [8] Haupt MC, Kowollik D, Lindhorst K, Hötte F. Fluid-structure-interaction in rocket thrust chambers simulation and validation. *Defect Diffusion Forum* 2016;366:97–117. <https://doi.org/10.4028/www.scientific.net/DDF.366.97>.
- [9] Fassin M, Kowollik D, Wulfinghoff S, Reese S, Haupt MC. Design studies of rocket engine cooling structures for fatigue experiments. *Arch Appl Mech* 2016;86(12):2063–93. <https://doi.org/10.1007/s00419-016-1160-6>.
- [10] Fiedler T, Rösler J, Bäker M. A new metallic thermal barrier coating system for rocket engines: failure mechanisms and design guidelines. *J Therm Spray Technol* 2019;28(7):1402–19. <https://doi.org/10.1007/s11666-019-00900-1>.
- [11] Deshpande S, Sampath S, Zhang H. Mechanisms of oxidation and its role in microstructural evolution of metallic thermal spray coatings-Case study for Ni-Al. *Surf Coat Technol* 2006;200(18–19):5395–406. <https://doi.org/10.1016/j.surfcoat.2005.07.072>.
- [12] Bose S. *High Temperature Coatings*, 1st ed. Amsterdam, The Netherlands: Elsevier; 2007.
- [13] Fiedler T, Groß R, Rösler J, Bäker M. Damage mechanisms of metallic HVOF-coatings for high heat flux application. *Surf Coat Technol* 2017;316:219–25. <https://doi.org/10.1016/j.surfcoat.2017.03.037>.
- [14] Fiedler T, Rösler J, Bäker M. Development of a CuNiCrAl bond coat for thermal barrier coatings in rocket combustion chambers. *J Therm Spray Technol* 2015;24(8):1480–6. <https://doi.org/10.1007/s11666-015-0325-0>.
- [15] Donachie MJ, Donachie SJ. *SUPERALLOYS A Technical Guide*, 2nd ed. Materials Park, OH: The Materials Information Society; 2002.
- [16] Bartz DR. A simple equation for rapid estimation of rocket nozzle convective heat transfer coefficient. *Jet Propul* 1957;27:49–51.
- [17] Gnielinski V. *Neue Gleichungen für den Wärme- und Stoffübergang in turbulent durchströmten Rohren und Kanälen*. *Forschung im Ingenieurwesen A* 1975;41(1):8–16.
- [18] Bauschinger J. Über die Veränderung der Elastizitätsgrenze und die Festigkeit des Eisens und Stahls durch Strecken und Quetschen, durch Erwärmen und Abkühlen und durch oftmals wiederholte Beanspruchungen, Mittheilungen aus dem Mechanisch-Technischen Laboratorium der Königlichen Technischen Hochschule in München, Vol. 13, No. 15; 1886.
- [19] Duval H. Investigation on Blanching on Cryogenic Engines Combustion Chamber Inner Liner, Ph.D. thesis, Ecole Centrale Paris, 11; 2014.
- [20] Ogbuji L. A table-top technique for assessing the blanching resistance of Cu Alloys. *Oxid Metals* 2005;63(5–6):383–99. <https://doi.org/10.1007/s11085-005-4393-2>.
- [21] Baukloh A, Drefahl K, Huebner U, Rühle M. *Zeitstandsuntersuchungen an niedrig- und unlegierten Kupferwerkstoffen*. *Metallwissenschaft und Technik* 1976;30:19–28.
- [22] Fiedler T, Rösler J, Bäker M. Large heat flux exposure of metallic coatings for rocket engine applications. *Surf Coat Technol* 2017;332:30–9. <https://doi.org/10.1016/j.surfcoat.2017.08.075>.